**Potential Anticancer Heterometallic Fe-Au and Fe-Pd Agents: Initial Mechanistic Insights**

*Nicholas Lease,[a] Vadim Vasilevski,[a] Monica Carreira,[a] Andreia de Almeida,[b] Mercedes Sanaú,[c] Pipsa Hirva,[d] Angela Casini,[b*] and Maria Contel[a*]*

**Supporting Information**

**Contents**:

**1. Crystallographic Data for Compounds 8 and 11**

**Table S1**. Crystal Data and Structure Refinement for Complexes **8** and **11**.

| **Compound** | **8** **[{(Cp-P(Ph$_2$)=N-CH$_2$-2-NC$_5$H$_4$)PdCl$_2$}Fe(Cp)].H$_2$O** | **11** **[(Ph$_3$P=N-CH$_2$-2-NC$_5$H$_4$)PdCl$_2$].CHCl$_3$** |
|---|---|---|
| formula | $C_{29}H_{29}Cl_2N_2OPPd$ | $C_{25}H_{22}Cl_5N_2PPd$ |
| fw | 685.66 | 543.26 |
| T [K] | 293(2) | 293(2) |
| $\lambda$ ($Mo_{K\alpha}$)[Å] | 0.71073 | 0.71073 |
| crystal system | triclinic | orthorhombic |
| space group | P-1 | Pbca |
| *a* [Å] | 9.942(2) | 13.102(3) |
| *b* [Å] | 11.730(2) | 14.328(3) |
| *c* [Å] | 13.316(3) | 15.347(3) |
| $\alpha$ [$^o$] | 85.63(3) | 90 |
| $\beta$ [$^o$] | 81.75(3) | 111.72(3) |
| $\chi$ [$^o$] | 65.43(3) | 90 |
| V [Å]$^3$ | 1397.4(5) | 2676.6(9) |
| Z | 2 | 4 |
| $D_{calcd}$ (g cm$^{-3}$) | 1.630 | 1.650 |
| $\mu$ (mm$^{-1}$) | 1.437 | 1.270 |
| GOF | 1.051 | 0.954 |
| $R_1[I > 2\sigma]$ | 0.0443 | 0.0375 |
| $wR_2$(all data) | 0.1368 | 0.0980 |

**2. DFT Studies for ligands 1-3, and 9 and for compounds 5-8 and 10, 11**

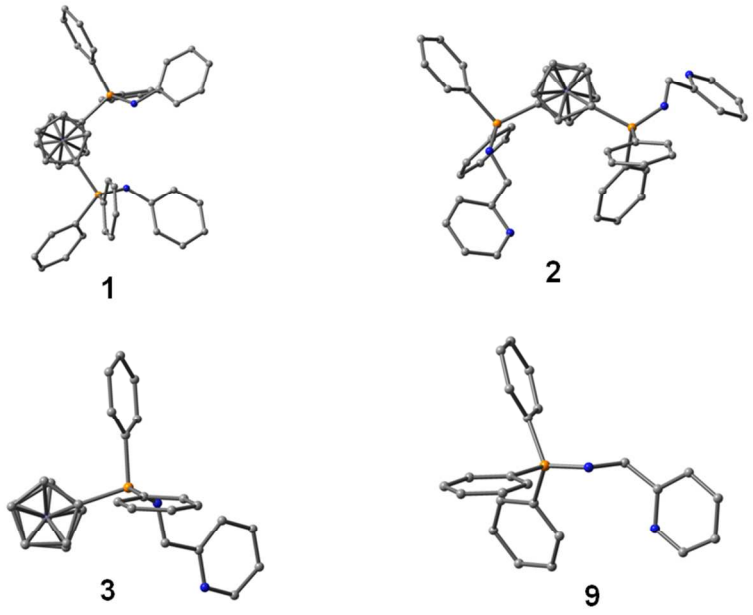


**Figure S1**. Optimized structures for the free ligands **1-3** and **9**. Hydrogens have been omitted for clarity. Note the conformation of the N-C-C-N torsion angle, and also the staggered conformation of the ferrocene rings in the doubly substituted ligands **1** and **2**.

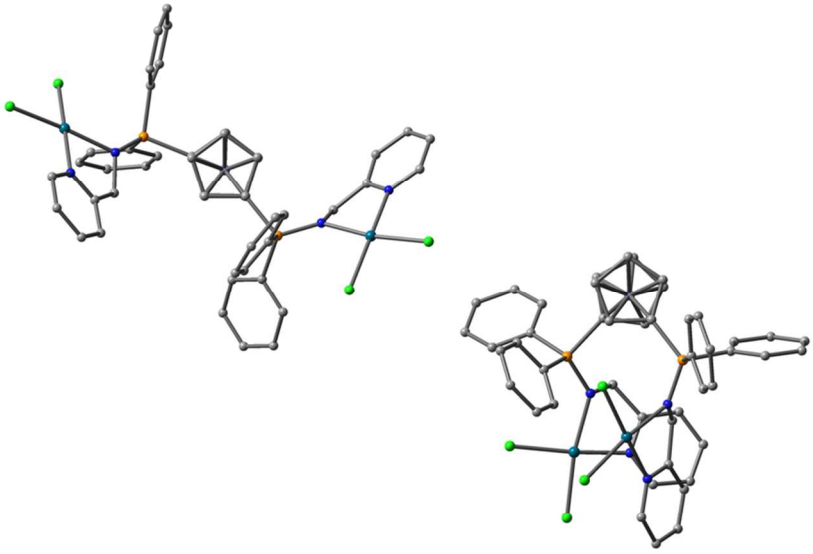

**Figure S2.** Comparison of the different substitution sites of the ferrocene rings to the optimized structure of palladium complex **6.** Left: substitution of 1,3' carbon sites; right: substitution of 1,2' carbon sites.

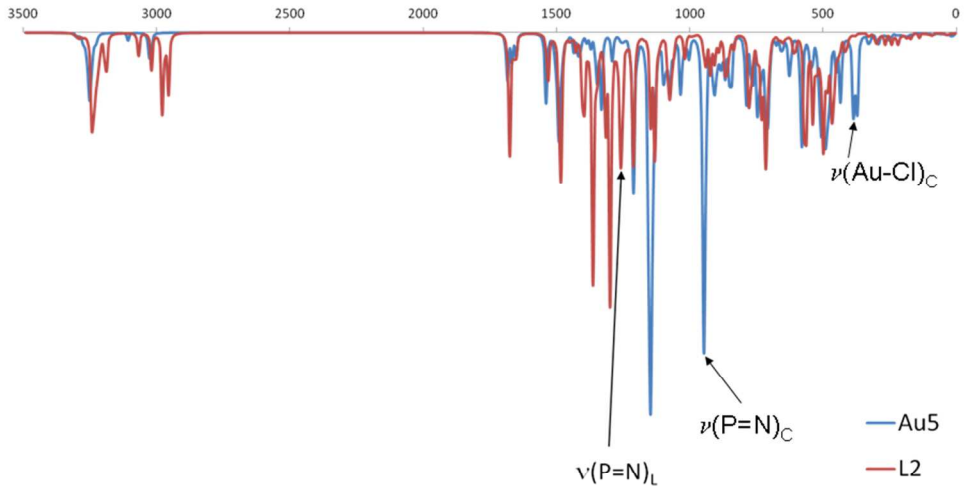


**Figure S3.** Computationally simulated IR spectrum of gold complex **5** and the corresponding free ligand **2**.

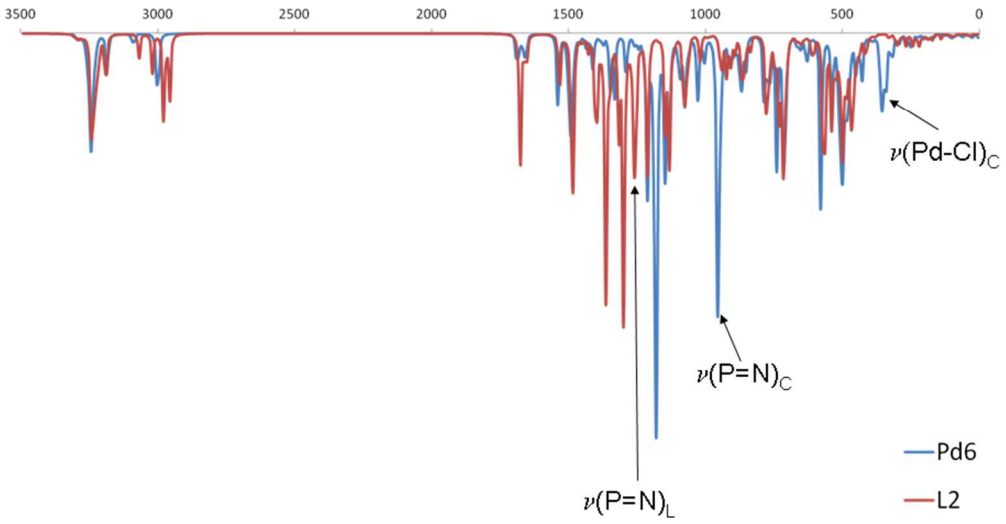


**Figure S4.** Computationally simulated IR spectrum of palladium complex **6** and the corresponding free ligand **2**.

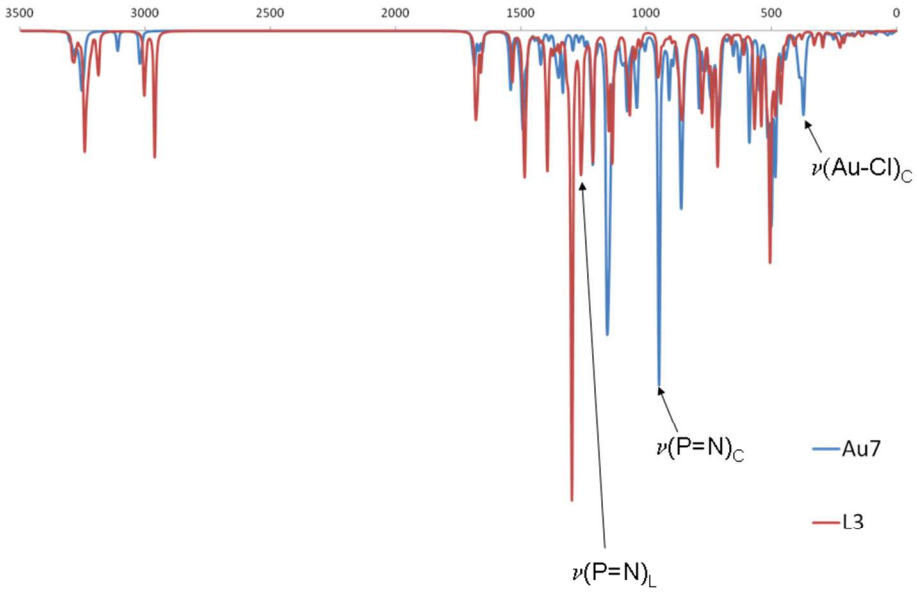


**Figure S5.** Computationally simulated IR spectrum of gold complex **7** and the corresponding free ligand **3**.

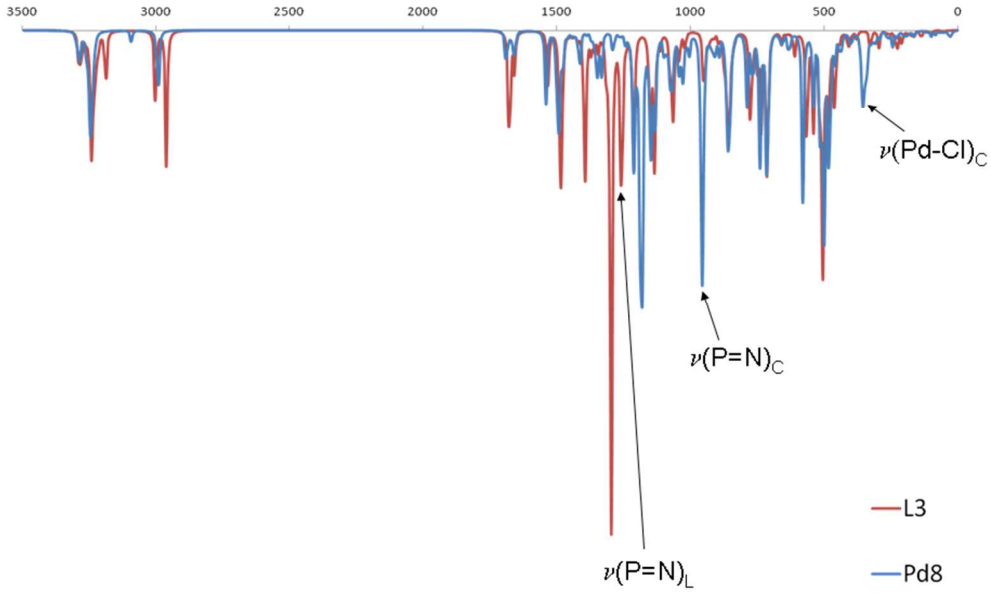


**Figure S6.** Computationally simulated IR spectrum of palladium complex **8** and the corresponding free ligand **3**.

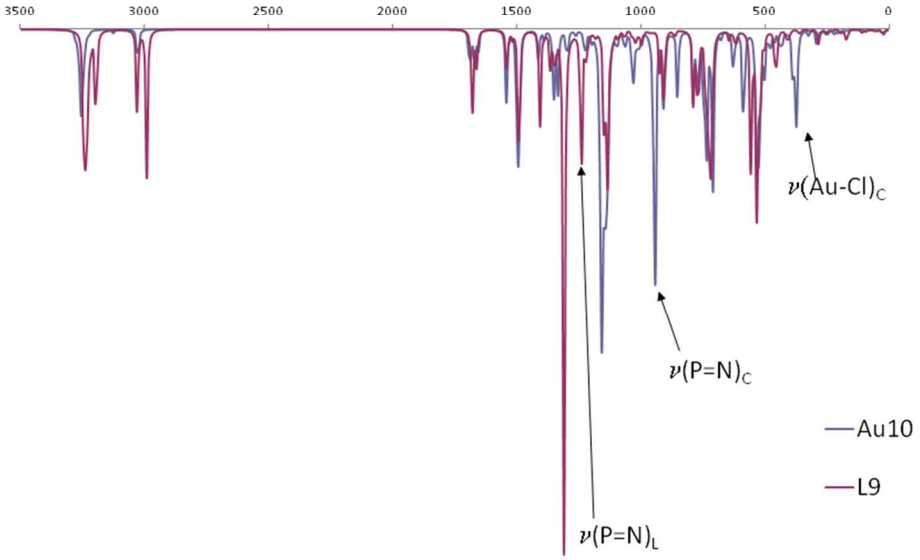


**Figure S7.** Computationally simulated IR spectrum of gold complex **10** and the corresponding free ligand **9**.

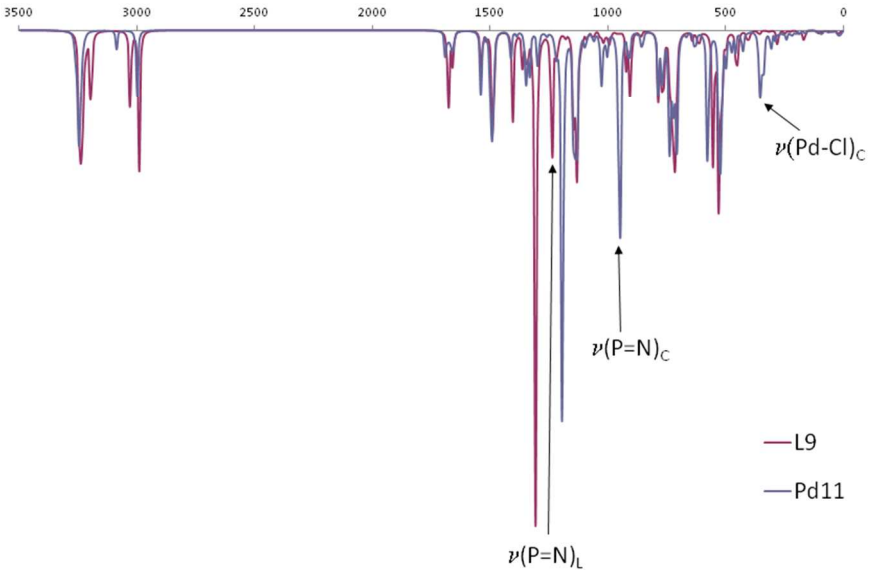


**Figure S8.** Computationally simulated IR spectrum of palladium complex **11** and the corresponding free ligand **9**.

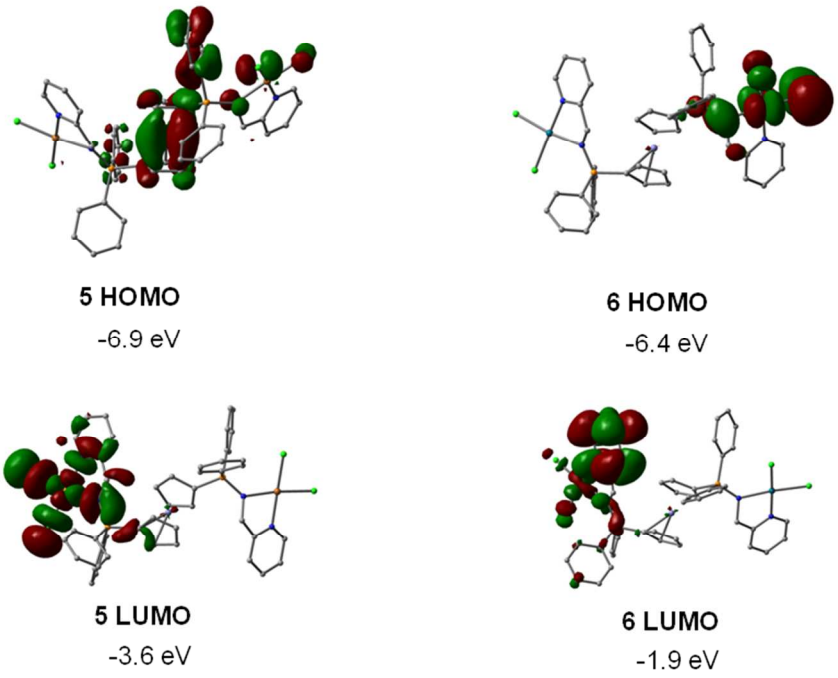


**Figure S9.** Selected frontier molecular orbitals for the gold complex **5** and the palladium complex **6**.

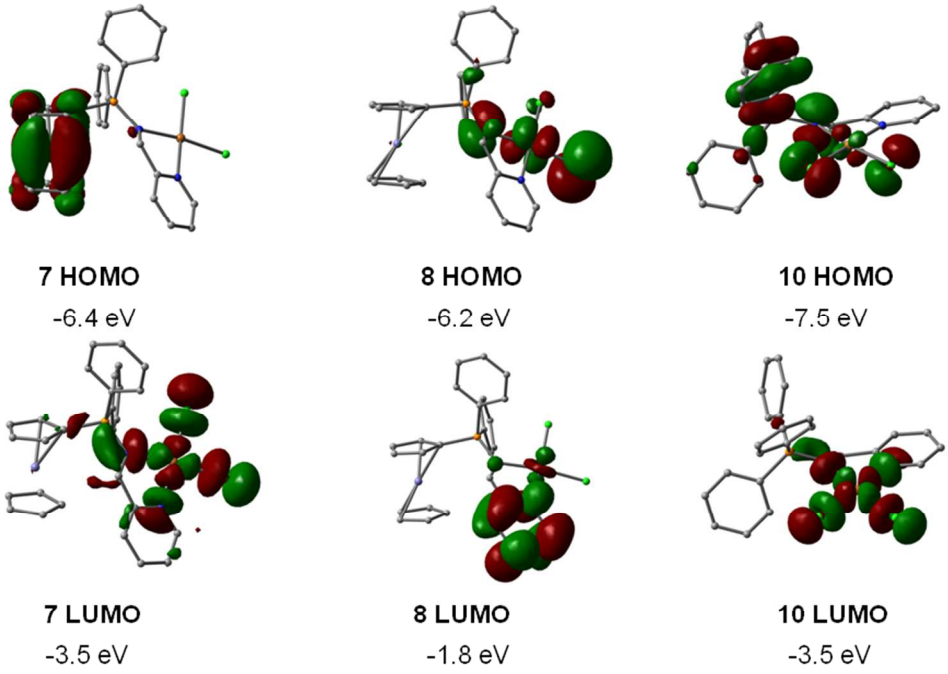


**Figure S10.** Selected frontier molecular orbitals for gold complexes **7** and **10**, and the palladium complex **8**.

**Calculation of the reaction energies**

The feasibility of the complexes was investigated by calculating the formation energies according to the reactions:

$x\ Au^{3+} + y\ Cl^- + L \Rightarrow [Au_xCl_yL]^{3x-y}$

$x\ Pd^{2+} + y\ Cl^- + L \Rightarrow [Pd_xCl_yL]$

The energies are reported as Gibbs free energy changes of the corresponding reactions (Table 1). The effect of the aqueous solution in the energy calculations was taken into account by a reaction field method, as explained in the Computational Details section. Table 1 (main text) lists also the HOMO-LUMO gaps, which can be regarded as a measure of the relative stability of the compounds.

When the HOMO-LUMO gaps were compared, the gold complexes showed smaller gaps, which is an indication of smaller chemical stability and hence larger reactivity of the gold complexes than the palladium ones. The main reason for the smaller stability is in the lower LUMO energies in the gold complexes. The appearance of the frontier molecular orbitals is presented in supplementary material (Figure S9). In general, the composition of the HOMO orbitals is different in the gold complexes than in the palladium ones. The HOMO of the palladium compounds mainly involves the metal d orbitals with a large contribution from the chlorine p orbitals, which is rather typical for transition metal complexes with halogen ligands. The LUMO orbital involves the $p^*$ system of the nitrogen ligand. In contrast, the HOMO of the gold complexes **5** and **7** both mainly consist of the bonding orbitals of the ferrocene fragment, which leads to destabilization of HOMO compared complex **10** with no ferrocene motif. The LUMO in all gold complexes is a combination of the metal d and the p orbitals of the halogens, which explains the large stabilization of the LUMO and the smaller energy gap.

## 3. $^{1}H$ and $^{13}C\{^{1}H\}$ NMR spectra for compounds 1, 3, 4, 5

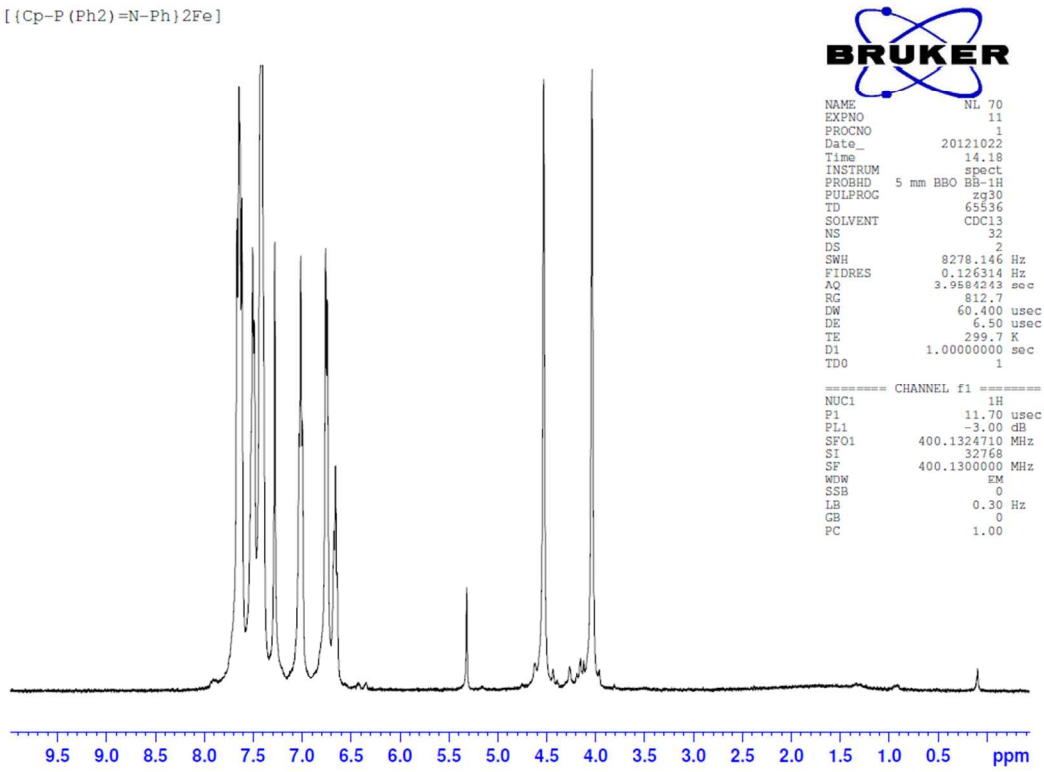


**Figure S11**. $^{1}H$ NMR spectra for ligand **1**.

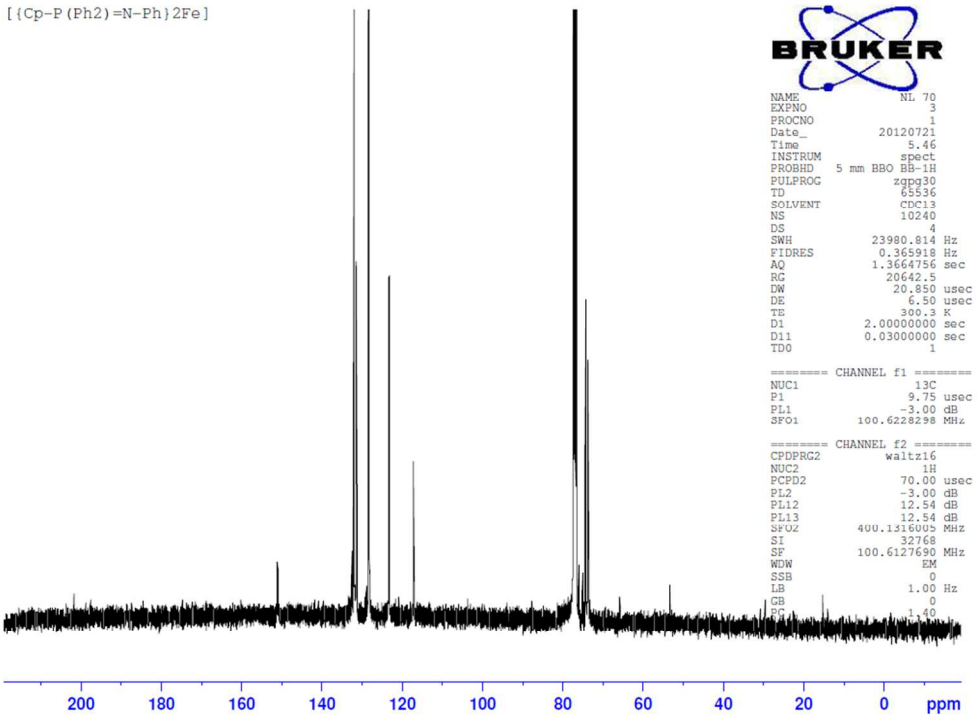


**Figure S12**. $^{13}C\{^{1}H\}$ NMR spectra for ligand **1**.

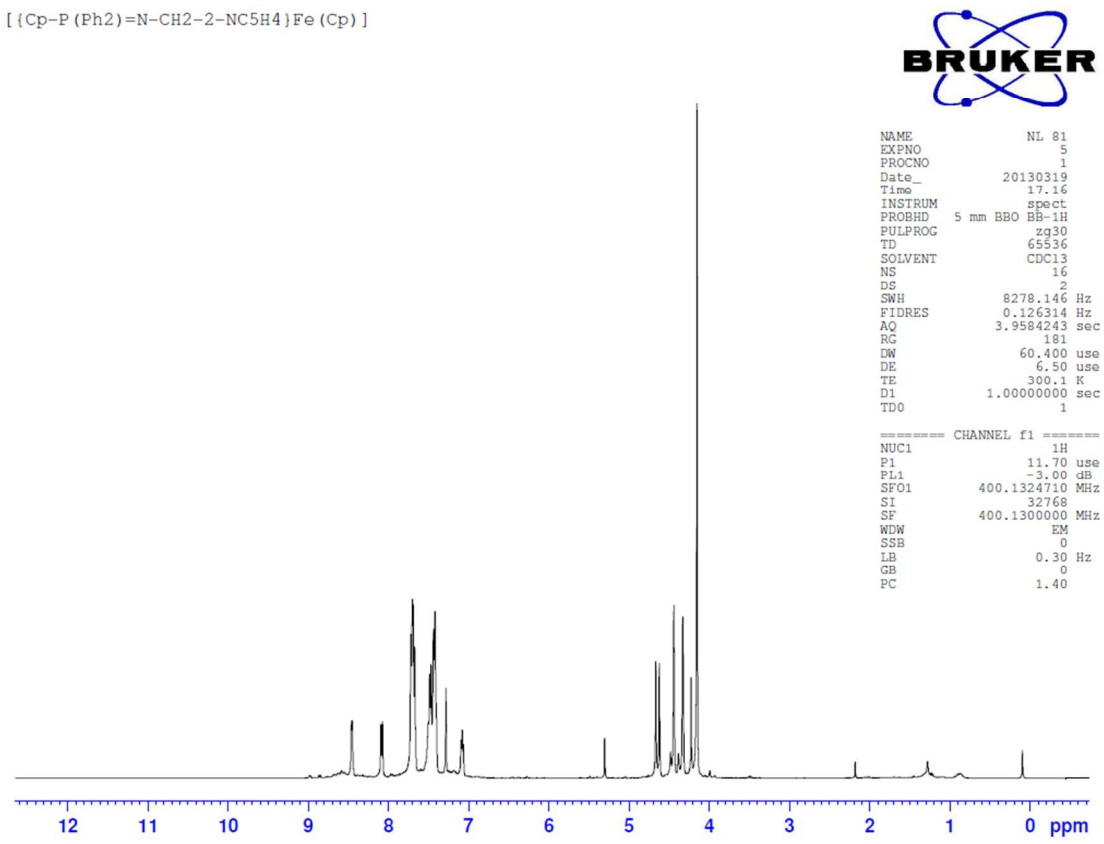


**Figure S13**. $^{1}$H NMR spectra for ligand **3**.

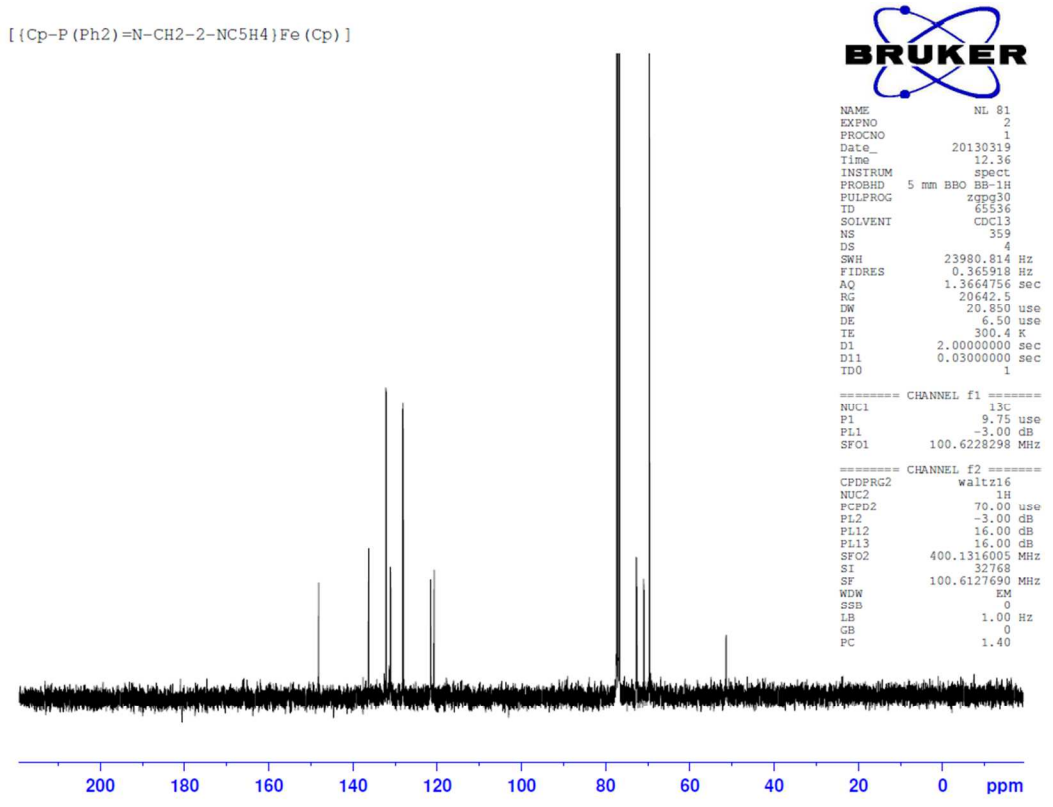


**Figure S14**. $^{13}$C{$^{1}$H} NMR spectra for ligand **3**.

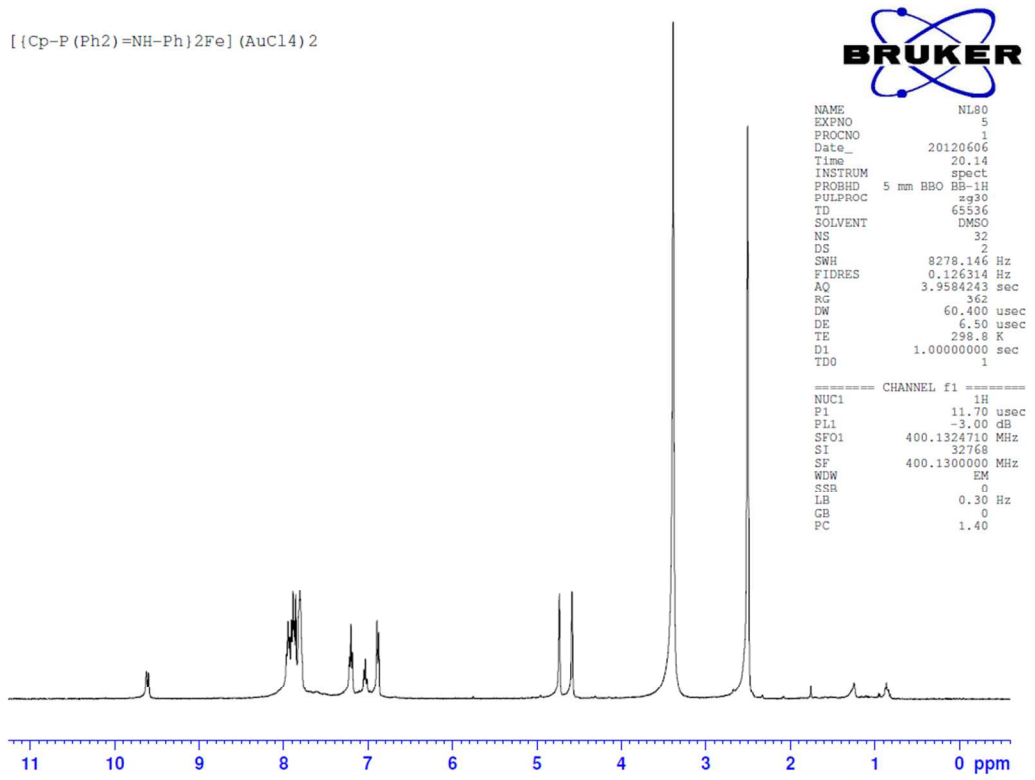


**Figure S15**. $^{1}$H NMR spectra for compound **4**

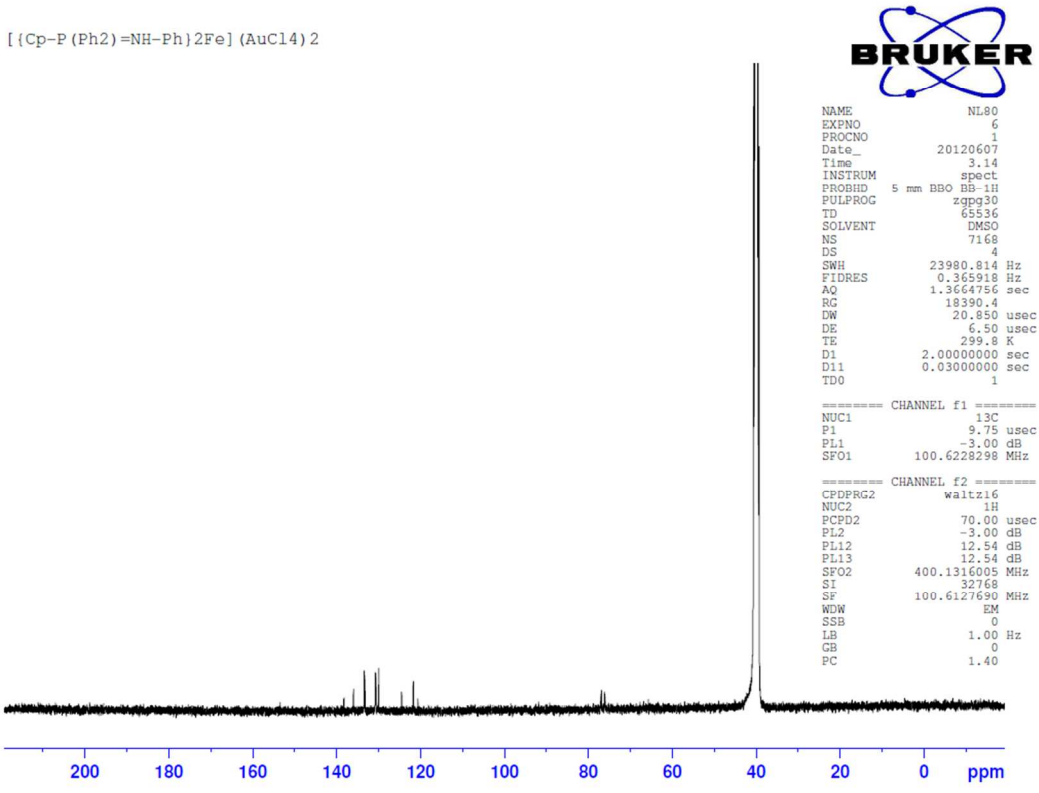


**Figure S16**. $^{13}$C{$^{1}$H} NMR spectra for compound **4**

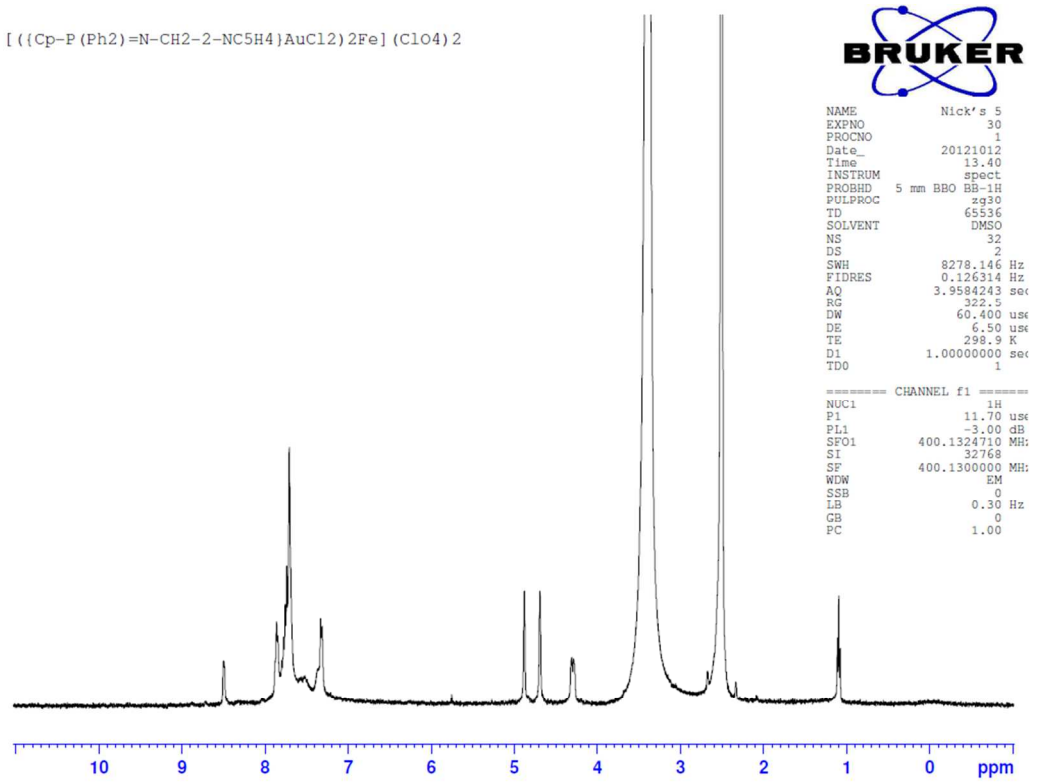


**Figure S17**. $^{1}$H NMR spectra for compound **5**

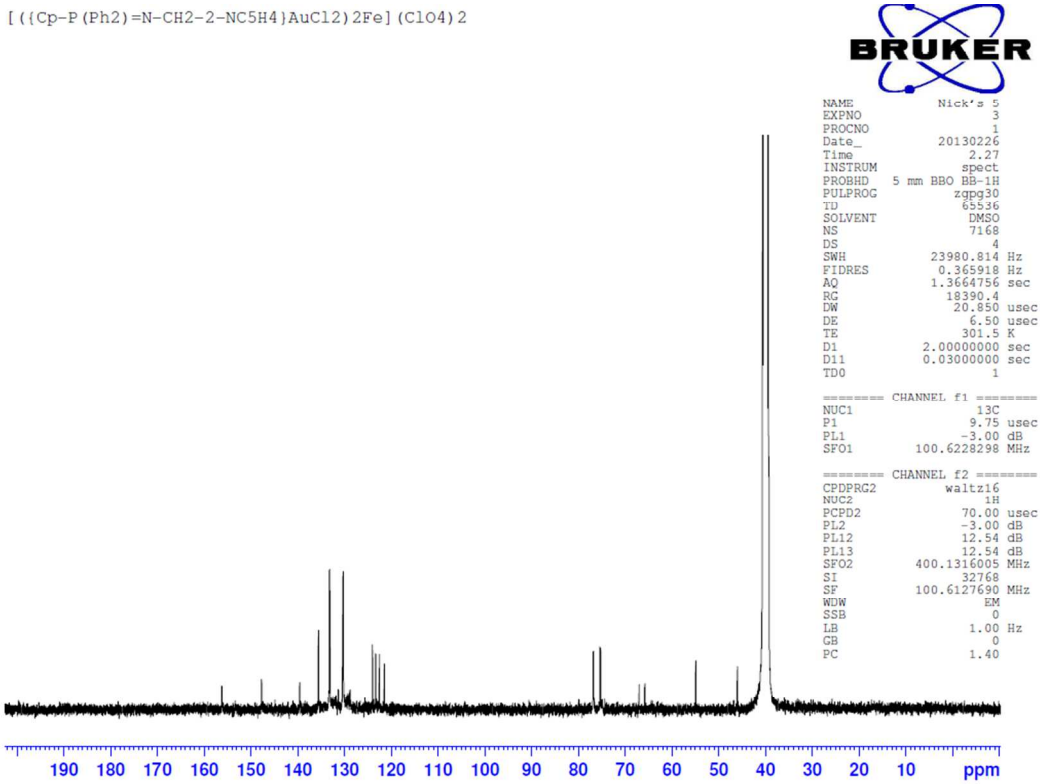


**Figure S18**. $^{13}$C{$^{1}$H} NMR spectra for compound **5**

**4. Stability of compounds 4-8, 10 and 11 in d$^6$-DMSO solution overtime assessed by $^{31}P\{^1H\}$ NMR spectroscopy.[a]**

| | d$^6$-DMSO | | | | |
|---|---|---|---|---|---|
| | 1 day | 4 days | 1 week | 2 weeks | Half life (50%) |
| **2** | 0% | | | | **10 min** |
| **3** | 0% | | | | **10 min** |
| **4** | >99% | >99% | >99% | | **weeks** |
| **5** | 92% | 82% | 80% | 72% | **weeks** |
| **6** | 80% | 50% | | | **4 days** |
| **7** | >99% | 75% | 45% | | **6 days** |
| **8** | 40% | 15% | 0% | | **20 hrs** |
| **10** | 15% | 0% | | | **4 hrs** |
| **11** | 67% | 40% | 20% | | **2.5 days** |

a) % of decomposition determined by integration of all the signals appearing in the $^{31}P\{^1H\}$ NMR spectra, the sum being set to 100%.

**5. Selected $^{31}P\{^1H\}$ NMR spectra showing the decomposition of compounds 5, 6, 10 in d$^6$-DMSO overtime**

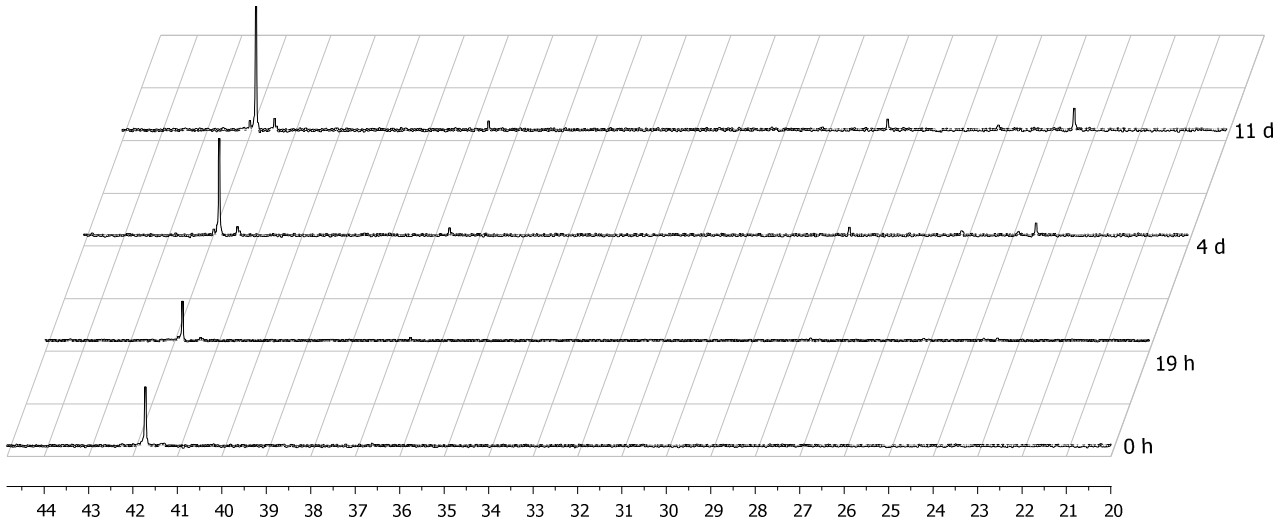


**Figure S19**. Selected $^{31}P\{^1H\}$ NMR spectra showing the decomposition of compound **5** in d$^6$-DMSO (δ 41.7) overtime.

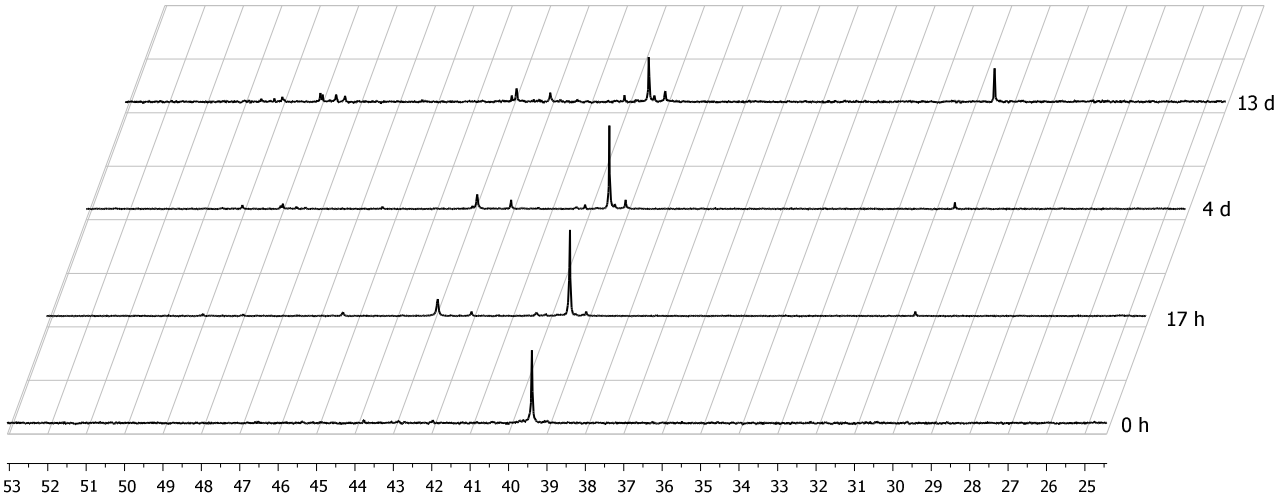


**Figure S20**. Selected $^{31}P\{^{1}H\}$ NMR spectra showing the decomposition of compound **6** in $d^6$-DMSO (δ 40.8) overtime.

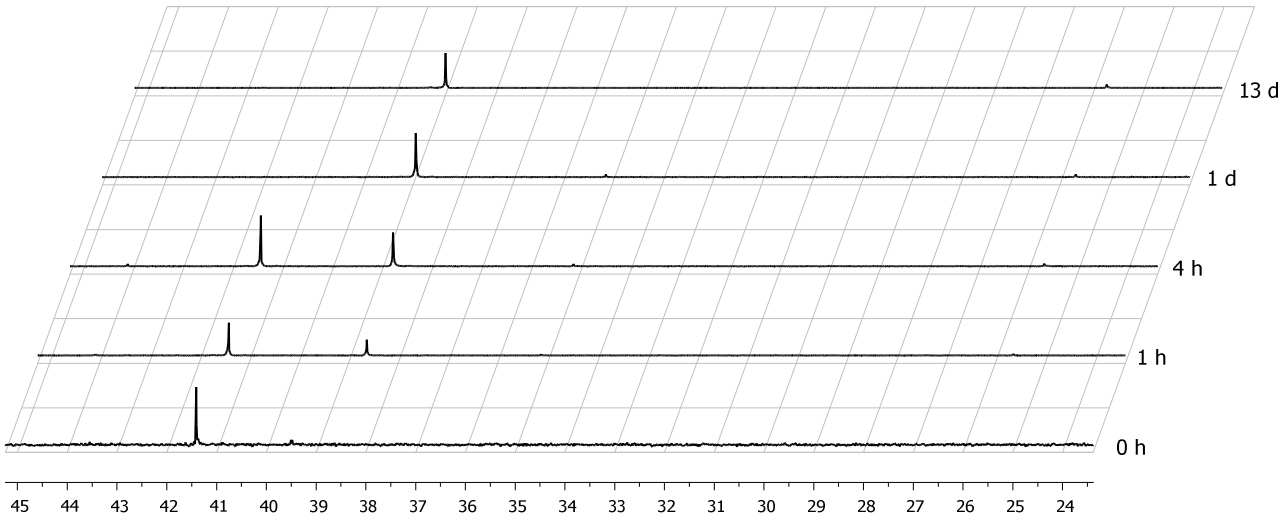


**Figure S21**. Selected $^{31}P\{^{1}H\}$ NMR spectra showing the decomposition of compound **10** in $d^6$-DMSO (δ 41.4) overtime.

**6. Selected UV-Vis spectra showing the decomposition of compounds 5, and 10 in PBS overtime**

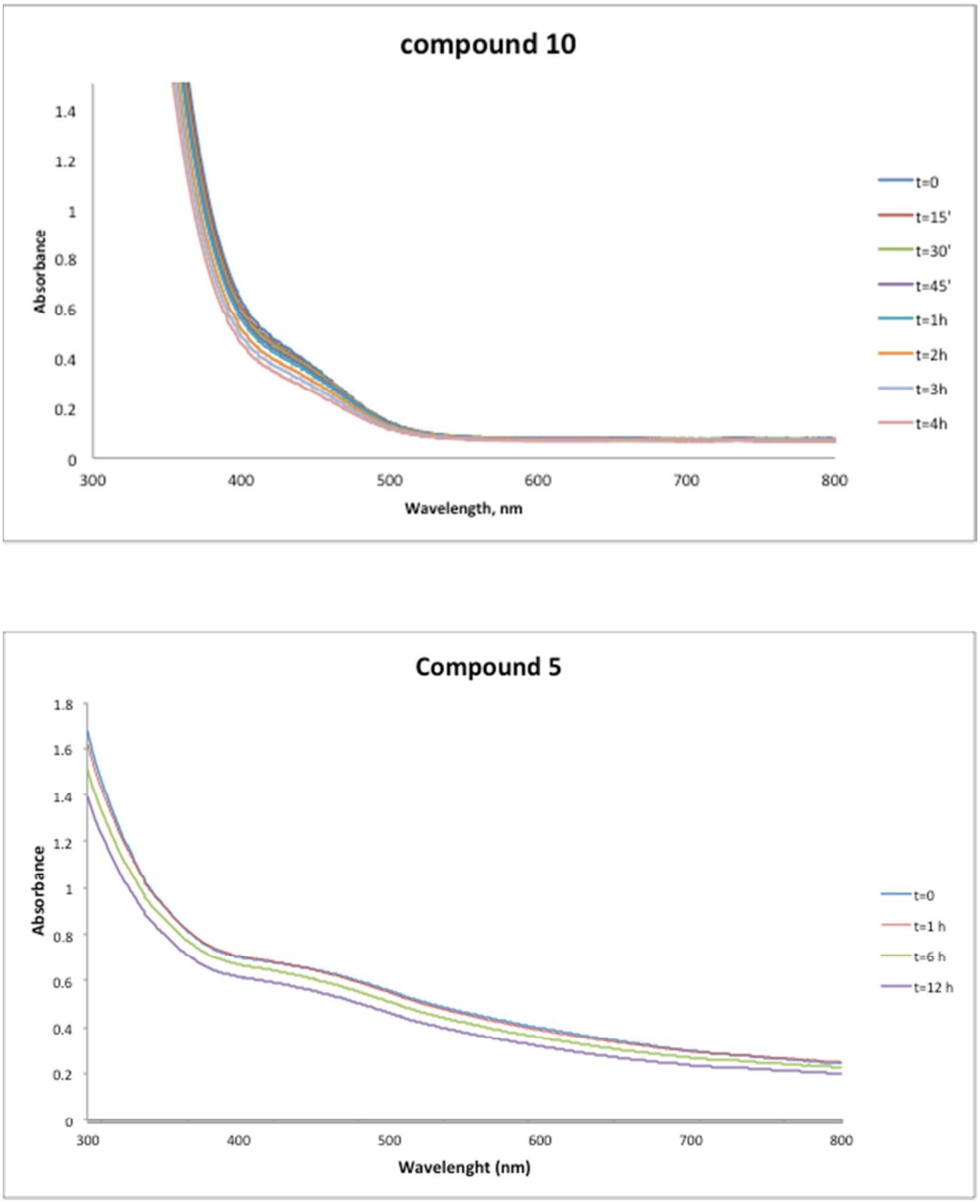


**Figure S22**. UV-visible spectra of compound **10** (mononuclear Au) ($10^{-3}$ M) and **5** (trimetallic Fe-$Au_2$) ($4x10^{-4}$ M) in PBS (pH 7.4) recorded over time, incubation at RT.